An embedded-atom method interatomic potential for Pd–H alloys

X.W. Zhou[a)] and J.A. Zimmerman
Mechanics of Materials Department, Sandia National Laboratories, Livermore, California 94550
B.M. Wong
Materials Chemistry Department, Sandia National Laboratories, Livermore, California 94550
J.J. Hoyt
Department of Materials Science and Engineering, McMaster University, Hamilton, Ontario, Canada L8S 4L7

(Received 19 September 2007; accepted 16 November 2007)

Palladium hydrides have important applications. However, the complex Pd–H alloy system presents a formidable challenge to developing accurate computational models. In particular, the separation of a Pd–H system to dilute (α) and concentrated (β) phases is a central phenomenon, but the capability of interatomic potentials to display this phase miscibility gap has been lacking. We have extended an existing palladium embedded-atom method potential to construct a new Pd–H embedded-atom method potential by normalizing the elemental embedding energy and electron density functions. The developed Pd–H potential reasonably well predicts the lattice constants, cohesive energies, and elastic constants for palladium, hydrogen, and PdH_x phases with a variety of compositions. It ensures the correct hydrogen interstitial sites within the hydrides and predicts the phase miscibility gap. Preliminary molecular dynamics simulations using this potential show the correct phase stability, hydrogen diffusion mechanism, and mechanical response of the Pd–H system.

I. INTRODUCTION

Palladium possesses the capacity to absorb a large amount of hydrogen to form a hydride.[1] This property enables many important applications such as hydrogen storage for clean portable energy, new refrigerator designs, catalytic converters, and nuclear radiation adsorption.[1–7] Palladium hydrides are also suited for safe and efficient processing of hydrogen isotopes such as tritium.[8–10] Materials used for these applications must have good mechanical properties. It is well known, however, that the dissolution of even a small amount of hydrogen in metals significantly deteriorates their properties, resulting in embrittlement, crack propagation, and corrosion.[11–13] There is another significant problem for the application of tritides caused by the natural radioactive decay of tritium to form helium atoms. These helium atoms are insoluble in palladium, and they tend to gather into bubbles of nanometric size.[14,15] The high bubble pressure exerts significant stresses that are large enough to cause lattice swelling, crack formation, and quick release of helium due to the coalescence of defects.[16,17] Understanding these phenomena is therefore critical to predict the time evolution (aging behavior) of material properties.

Hydrogen can be continuously pumped into the palladium lattice as the surrounding hydrogen gas pressure is increased. As the hydrogen content increases, the solid solution first forms a low hydrogen concentration α phase and then a high hydrogen concentration, but more defective β phase. In both α and β phases, palladium atoms fully occupy a face-centered-cubic (fcc) lattice, whereas hydrogen atoms partially occupy the octahedral interstitial sites of the palladium lattice. The pressure–composition curve exhibits a plateau (isotherm) in an intermediate composition regime where α and β phases coexist. At room temperature and ambient pressure, the α and β phases exist at approximate concentrations of $H/Pd = 0.03$ and 0.60, respectively.[18]

The pressure–composition isotherm is a central phenomenon for the application of the hydride[19] and may also affect mechanical properties. For instance, inserting hydrogen into the octahedral sites of the palladium fcc lattice expands the lattice in linear proportion to the hydrogen content.[2] The dislocation density increases during the hydriding process for accommodating the lattice

---

[a)] Address all correspondence to this author.
e-mail: xzhou@sandia.gov
DOI: 10.1557/JMR.2008.0090

© 2008 Materials Research Society

distortion induced by the coexistence of phases, thereby causing the emergence of fracture.[20]

The technological importance has stimulated an interest to model PdH$_x$ hydride. Extensive first-principles calculations have been carried out.[6] Larger-scale molecular dynamics (MD) or Monte Carlo (MC) simulations have not been widely used because of the lack of a high-fidelity Pd–H interatomic potential that is applicable to the hydrogen composition range $0 \leqslant x \leqslant 1$ and is capable of predicting the pressure–composition isotherm (i.e., the α and β phase miscibility gap). Numerous Pd–H potentials have been developed.[21–24] However, these potentials are mainly designed for dilute hydrogen compositions, and none of them have been found to correctly predict the miscibility gap. Some potentials even incorrectly predict the occupancy of tetrahedral interstitial sites by hydrogen atoms.

To our knowledge, the Pd–H embedded-atom method (EAM) interatomic potential developed by Wolf et al. is the only one that has been successfully used in MC simulations to qualitatively predict the pressure–composition isotherm.[25] However, in their 1993 publication the authors do not present the functions and parameters that dictate the Pd–H and H–H interactions; rather, they refer only to their earlier 1992 publication[26] that presents information only on an EAM potential for pure palladium. Extensive efforts have been made to obtain this information,[27] but to our knowledge, specifics on the potential have been lost. In addition, no testing of this potential with regard to mechanical properties, e.g., elastic constants and tensile and shear strengths, has been performed.

The purpose of the present work is to develop a Pd–H interatomic potential that is applicable to the entire hydrogen composition range $0 \leqslant x \leqslant 1$ and is capable of predicting the miscibility gap. Details regarding how model functions and parameters were obtained are described, and physical and mechanical properties of the resulting potential are explored.

II. EAM

While there are a variety of mathematical formalisms for interatomic potentials, the EAM potential has an advantage of being both computationally efficient and suited to fcc metal systems. EAM potential was initially developed by Daw and Baskes.[21,22] It improves over pair potentials by incorporating the environmental dependence of the atomic interactions. As a result, it has been successfully applied to a variety of metal and metal alloy systems.[28,29] EAM has also been successfully applied in some of the metal hydride problems.[30] EAM is hence chosen as the format for our Pd–H potential.

In EAM, the cohesive energy of a computational system composed of N atoms is expressed as

$$E_c = \frac{1}{N} \cdot \left(\sum_{i=1}^{N} F_i(\rho_i) + \frac{1}{2} \cdot \sum_{i=1}^{N} \sum_{\substack{j=1 \\ j \neq i}}^{N} \phi_{ij}(r_{ij}) \right) \quad , \tag{1}$$

where $F_i(\rho_i)$ is an embedding energy at site of atom i with a background electron density of ρ_i, and $\phi_{ij}(r_{ij})$ is a pair energy between atoms i and j separated by a distance r_{ij}. Electron density at the site of atom i is calculated as

$$\rho_i = \sum_{\substack{j=1 \\ j \neq i}}^{N} \rho_j^a(r_{ij}) \quad , \tag{2}$$

where $\rho_j^a\ (r_{ij})$ is the electron density contribution from atom j that is r_{ij} away from site i. This EAM potential requires three functions for each element (e.g., i = Pd, H): the embedding energy $F_i(\rho)$ as a function of electron density ρ, the pair energy $\phi_{ii}(r)$ as a function of atom distance r, and the atomic electron density $\rho_i^a\ (r)$ as a function of atom distance r. In addition to these three functions for each of the elements, the cross-pair energy between dissimilar species i and j, $\phi_{ij}(r)$, is required for the alloy system.

III. PALLADIUM POTENTIAL

Numerous EAM potentials have already been developed for palladium.[23,28,31] All of these potentials well captured the properties of palladium. In particular, the potential developed by Foiles and Hoyt,[32] which incorporates the universal equation of state derived by Rose et al.,[33] reproduces exactly the experimental lattice constant, cohesive energy, and bulk modulus of the fcc palladium crystal. It also well predicts other elastic constants, vacancy formation energy and its relaxation volume, various defect energies and their relaxation volumes, defect migration energies, stacking fault energies, and various surface energies and surface relaxations. These properties are important for capturing the mechanical properties of palladium. The same palladium EAM potential has also been used to successfully study the effects of helium bubbles in palladium matrix.[32,34] As a result, we construct our Pd–H potential based on this palladium EAM potential. This palladium potential is available in tabular form and is included in molecular dynamics simulation packages released from Sandia National Laboratories.[35] For convenience, we also fitted the tabular palladium functions with high-order polynomial functions and the results are shown in the Appendix.

The EAM potential has a special property in that an elemental EAM potential is invariant to a transformation to the embedding energy function,

$$G(\rho) = F(\rho) + k \cdot \rho \quad , \tag{3}$$

and a concurrent transformation to the pair potential

$$\psi(r) = \phi(r) - 2k \cdot \rho^{a}(r) \quad , \tag{4}$$

where k is an arbitrary constant. While k does not change the properties of the element, it does change the properties of the alloys when the elemental potentials are combined.[21,36–38] During potential parameterization, an optimization procedure is used to minimize an objective function defined as the sum of the square deviation of predicted properties from the corresponding target (either experimental or ab initio calculated) properties. At first sight, it appears that k can be treated as a fitting parameter so that the formulism has more freedom to better minimize the objective function. However, we found that this scheme caused a drift of k to unphysical values, resulting in potentials that failed to predict the stable alloy crystal structures during MD simulations even though these structures were statically well fitted. This problem can be overcome by uniquely defining k using a normalization condition that requires the equilibrium to be independently achieved for embedding and pair energy functions for the most stable elemental crystal phase. By setting the first derivative of the embedding energy to 0, k can be solved and the normalized palladium embedding and pair energy functions are expressed as

$$F_{\mathrm{Pd}}(\rho) = F_{\mathrm{Pd,u}}(\rho) + F'_{\mathrm{Pd,u}}(\rho_{0,\mathrm{Pd}}) \cdot \rho \quad , \tag{5}$$

$$\phi_{\mathrm{PdPd}}(r) = \phi_{\mathrm{PdPd,u}}(r) - 2 \cdot F'_{\mathrm{Pd,u}}(\rho_{0,\mathrm{Pd}}) \cdot \rho^{a}_{\mathrm{Pd}}(r) \quad , \tag{6}$$

where $F_{\mathrm{Pd,u}}(\rho)$ and $\phi_{\mathrm{PdPd,u}}(r)$ are the original (unnormalized) palladium embedding and pair energy functions,[32] $F'_{\mathrm{Pd,u}}(\rho_{0,\mathrm{Pd}})$ is the first derivative of the original palladium embedding energy evaluated at the equilibrium electron density of the most stable crystal phase of palladium, $\rho_{0,\mathrm{Pd}}$, and $F_{\mathrm{Pd}}(\rho)$ and $\phi_{\mathrm{PdPd}}(r)$ are the corresponding normalized functions used in the present work. $\rho_{0,\mathrm{Pd}}$ is equal to a value of 10.261 as determined by using Eqs. (2) and (A2) and assuming a fcc crystal structure at a lattice constant of 3.885 Å.

IV. HYDROGEN POTENTIAL AND PAIR INTERACTION BETWEEN PALLADIUM AND HYDROGEN

With the palladium potential known, the remaining work is to develop a hydrogen potential and a cross-pair potential between palladium and hydrogen. It is more convenient to use analytical expressions. The pair potential is approximated by

$$\begin{aligned}\phi_{\mathrm{HH}}(r) = D_{\mathrm{HH}} \cdot (\beta_{\mathrm{HH}} \cdot \exp[-\alpha_{\mathrm{HH}}(r - r_{0,\mathrm{HH}})] \\ - \alpha_{\mathrm{HH}} \cdot \exp[-\beta_{\mathrm{HH}}(r - r_{0,\mathrm{HH}})]) \quad ,\end{aligned} \tag{7}$$

where D_{HH}, α_{HH}, β_{HH}, and $r_{0,\mathrm{HH}}$ are four positive constants, and in particular, $r_{0,\mathrm{HH}}$ represents the equilibrium bond length of a dimer, and D_{HH} ($\beta_{\mathrm{HH}} - \alpha_{\mathrm{HH}}$) is its binding energy. Equation (7) well approximates the pair energy because it is more general than a Morse potential, with the latter being a special case of Eq. (7) at $\alpha_{\mathrm{HH}}/\beta_{\mathrm{HH}} = 2$.

Within the interaction range usually encountered in atomistic simulations, electron density increases as atomic separation decreases. An exponential decay function well captures this behavior and is used to approximate the hydrogen electron density function:

$$\rho^{a}_{\mathrm{H}}(r) = C_{\mathrm{H}} \cdot \exp[-\delta_{\mathrm{H}} \cdot r] \quad , \tag{8}$$

where C_{H} and δ_{H} are two positive constants.

The embedding energy must have a zero value at zero electron density where atoms are far separated. Previously used embedding energy functions are usually constructed by further requiring that they have a negative slope at small electron densities and a positive slope at large electron densities.[21,22] The function $F(\rho) = A_1 \cdot \rho \cdot \ln(\rho) + A_2 \cdot \rho$ satisfies these requirements, where A_1 (>0) and A_2 are two constants. A problem with this function is that it has a negative infinity slope at the point $\rho = 0$. Here we use an embedding energy function form that has a finite negative slope at $\rho = 0$ and a positive slope at large electron densities. It is expressed as

$$\begin{aligned}F_{\mathrm{H,u}}(\rho) = -c_{\mathrm{H}} \cdot \Bigg(\frac{1}{2 + d_{\mathrm{H}}} \cdot (\rho + \epsilon_{\mathrm{H}})^{2+d_{\mathrm{H}}} - \frac{a_{\mathrm{H}} + b_{\mathrm{H}}}{1 + d_{\mathrm{H}}} \\ \cdot (\rho + \epsilon_{\mathrm{H}})^{1+d_{\mathrm{H}}} + \frac{a_{\mathrm{H}} \cdot b_{\mathrm{H}}}{d_{\mathrm{H}}} \cdot (\rho + \epsilon_{\mathrm{H}})^{d_{\mathrm{H}}} \Bigg) \quad ,\end{aligned} \tag{9}$$

where a_{H}, b_{H}, c_{H}, d_{H}, and ϵ_{H} are five positive constants. It can be seen that when $\epsilon_{\mathrm{H}} = 0$, a_{H} is the electron density at which the embedding energy is a minimum, and as long as b_{H} is larger than any electron density that can be encountered during simulations, Eq. (9) does not have other minimum or maximum points within the electron density range simulated. The parameter d_{H} is introduced to make the function more flexible to better fit the material properties. Because when we use the polynomial functions described in the Appendix, it is possible that electron density becomes slightly negative at the cutoff distance of the potential. We therefore introduce a small positive number $\epsilon_{\mathrm{H}} = 0.0540638$ to ensure that Eq. (9) is defined in all atomic spacings. Note that Eq. (9) is not a normalized function because its slope does not naturally equal 0 at the equilibrium electron density. It is therefore normalized by

$$F_{\mathrm{H}}(\rho) = F_{\mathrm{H,u}}(\rho) - F'_{\mathrm{H,u}}(\rho_{0,\mathrm{H}}) \cdot \rho \quad . \tag{10}$$

Because the overall potential is fitted to equilibrium structure, the pair potential is automatically normalized once the embedding energy is normalized.

The EAM model described previously has another special property in that the elemental potential remains invariant to a transformation to the electron density contribution function

$$\mu_H^a(r) = \rho_t \cdot \rho_H^a(r) \quad , \tag{11}$$

as long as a concurrent transformation is made to the embedding energy

$$G_H(\rho) = F_H(\rho/\rho_t) \quad , \tag{12}$$

where ρ_t is an arbitrary constant, and $\mu^a{}_H$ and G_H are the transformed functions. This arises because the electron density is defined in a relative unit. While ρ_t does not affect elemental properties, it does affect the alloy properties. Again we found that ρ_t cannot be treated as a fitting parameter as the minimization of the objective function causes it to drift to an unphysical value that fails to stabilize the fitted crystal structures during MD simulations. It is recognized that the equilibrium electron densities of different elements must be measured in the same unit. While their values are most likely to be different, they should not differ by orders of magnitude. We can therefore normalize the electron density by imposing the constraint

$$\rho_{min} \leqslant \rho_{0,i} \leqslant \rho_{max} \quad , \tag{13}$$

where $\rho_{0,i}$ is the equilibrium electron density in the most stable crystal structure of element i, and ρ_{min} and ρ_{max} are lower and higher bounds for electron density that is common to all elements. This approach does not specifically define ρ_t, but with proper electron density bounds, Eq. (13) ensures that the electron density units of different elements are compatible at least in terms of order of magnitude, and it also provides sufficient freedom for each element to adjust its own electron density. Given the value of $\rho_{0,Pd}$ stated earlier, we used the values of $\rho_{min} = 3$ and $\rho_{max} = 14$. ρ_t is taken to be equal to 1. We found that with the two normalizations described previously, well-behaved alloy potentials were always obtained.

Finally, the cross-pair potential between palladium and hydrogen is simply approximated by the generalized Morse potential discussed previously,

$$\begin{aligned}\phi_{PdH}(r) = D_{PdH} \cdot (\beta_{PdH} \cdot \exp[-\alpha_{PdH}(r - r_{0,PdH})] \\ - \alpha_{PdH} \cdot \exp[-\beta_{PdH}(r - r_{0,PdH})]) \quad .\end{aligned} \tag{14}$$

V. PALLADIUM–HYDROGEN SOLID-SOLUTION MODEL

A. Gibbs free energy of mixing

The phase miscibility is determined by the Gibbs free energy of mixing per atom as a function of composition in units of mol fraction. Here we first examine the function of Gibbs free energy of mixing.

The Gibbs free energy of mixing is expressed as

$$\Delta G^{mix} = \Delta H^{mix} - \Delta S^{mix} \cdot T \quad , \tag{15}$$

where ΔH^{mix} and ΔS^{mix} are enthalpy and entropy of mixing (per atom), respectively, and T is the temperature. The reference materials of the mixing can be arbitrary, but here it is convenient to define the mixing as the process of forming PdH_x from two reference materials palladium and PdH. Consider the mixing reaction

$$[N_{Pd} \cdot x]PdH + [N_{Pd} \cdot (1 - x)]Pd \rightarrow [N_{Pd}]PdH_x \quad , \tag{16}$$

where N_{Pd} is total number of Pd atoms involved in the mixing. As can be seen, the factors $N_{Pd} \cdot x$, $N_{Pd} \cdot (1 - x)$, and N_{Pd} in Eq. (16) represent the numbers (chemical formula units) of the three corresponding materials PdH, palladium, and PdH_x. Assuming that the cohesive energies (per atom) for PdH, palladium, and PdH_x are E_{PdH}, E_{Pd}, and E_{PdH_x}, respectively, the total change of energy for Eq. (16) is

$$\begin{aligned}\Delta E_t = N_{Pd} \cdot (1 + x) \cdot E_{PdH_x} - 2 \cdot N_{Pd} \cdot x \cdot E_{PdH} \\ - N_{Pd} \cdot (1 - x) \cdot E_{Pd} \quad .\end{aligned} \tag{17}$$

The change of energy per atom is then

$$\begin{aligned}\Delta E = [(1 + x) \cdot E_{PdH_x} - 2 \cdot x \cdot E_{PdH} \\ - (1 - x) \cdot E_{Pd}]/(1 + x) \quad .\end{aligned} \tag{18}$$

Replacing x with mol fraction $X = x/(1+x)$, we have the heat of mixing

$$\Delta H^{mix} = E_{PdH_x} - 2 \cdot X \cdot E_{PdH} - (1 - 2 \cdot X) \cdot E_{Pd} \quad , \tag{19}$$

which is consistent with the conventional definition of heat of mixing.[39,40]

The entropy of mixing can be approximated by the change of the configurational entropy. The PdH_x lattice is composed of two sublattices occupied by palladium and hydrogen atoms, respectively. There is no configurational entropy on the palladium sublattice as it is fully occupied. The hydrogen sublattice can be viewed as forming a substitutional H-vacancy "alloy." The total configurational entropy of the hydrogen sublattice is then

$$\Delta S_t = -N_{Pd} \cdot k_B \cdot (x \cdot \ln[x] + (1 - x) \cdot \ln[1 - x]) \quad , \tag{20}$$

where k_B is Boltzmann constant. Notice that the total number of palladium atoms N_{Pd} equals the total number of sublattice sites (i.e., the total number of hydrogen atoms and vacancies). The configurational entropy per atom is then

$$\Delta S = -k_B \cdot (x \cdot \ln[x] + (1 - x) \cdot \ln[1 - x])/(1 + x) \quad , \tag{21}$$

Again replacing x with mol fraction X, we have an entropy of mixing expression

$$\Delta S^{\mathrm{mix}} = -k_B \cdot (X \cdot \ln[X/(1 - X)] + (1 - 2 \cdot X) \cdot \ln[(1 - 2 \cdot X)/(1 - X)]) \quad . \tag{22}$$

Equations (15), (19), and (22) define a Gibbs free energy of mixing. It should be noted that in classic molecular dynamics simulations, the heat capacity is approximated as independent of materials. In that case, the temperature does not affect heat of mixing. As a result, Eq. (19) can be used for other temperatures even if it is derived at 0 K.

B. Cohesive energy as a function of composition

While the cohesive energy of any phase can be calculated from the interatomic potential and Eq. (1) using a computational system, the approach is too computationally expensive when applied for a wide range of compositions and different structures (e.g., fcc palladium with hydrogen at octahedral as well as tetrahedral interstitial sites). Here we use a solid-solution model to derive an approximate analytical equation for cohesive energy as a function of composition and structure. This solid-solution model assumes an ideally random distribution of atoms so that each palladium or hydrogen atom sees the same environment. While this model greatly improved the calculation efficiency, it also produced results that were sufficiently close to those obtained from MD simulations of real systems.

At first sight, it was not clear whether hydrogen needed to be included in the potential parameterization, as our goal is to model various compositions of the PdH_x alloy system rather than solid or molecular hydrogen. However, we found that if hydrogen properties were not included in the parameterization, the minimization of the objective function almost always drove the hydrogen cohesive energy to an unrealistically high magnitude, resulting in abnormal hydrogen segregation that distorted and unstabilized the fitted alloy phases during MD simulations. Here, we derive a cohesive energy equation that includes the hydrogen phase. For this purpose, we use a more general chemical formula for our compound system, Pd_yH_x, so that it includes both hydrogen ($y = 0$, $x = 1$) and PdH_x ($y = 1$) phases.

In the formulation of Gibbs free energy of mixing described previously, we considered only the equilibrium PdH_x structure where hydrogen atoms occupy the octahedral interstitial sites of the palladium lattice. During the fitting of the cohesive energy, it is important to ensure that this equilibrium phase has the lowest cohesive energy. This means that the cohesive energies of both equilibrium and nonequilibrium phases must be included in the fitting. For this purpose, we assume a general Pd_yH_x lattice containing several fcc sublattices, where palladium atoms occupy one fcc sublattice and hydrogen atoms occupy other fcc sublattices. Two structures considered are shown in Fig. 1, where in Fig. 1(a), hydrogen atoms occupy the octahedral interstitial sites, and in Fig. 1(b) hydrogen atoms occupy the tetrahedral interstitial sites. Accordingly, we denote the structures shown in Figs. 1(a) and 1(b) by "OC" and "TE," respectively. It can be seen that there is only one fcc sublattice for the octahedral interstitial sites so that the maximum composition for the OC structure is $x = 1$ (note that x can also be viewed as the occupancy probability on the sublattice). On the other hand, there are two fcc sublattices for the tetrahedral interstitial sites so that the maximum composition for the TE structure is $x = 2$. Alternatively, we can also represent the OC and TE structures by specifically including the number of hydrogen sublattices in the chemical formulae so that they become PdH_x and $PdH_{x/2}H_{x/2}$, respectively. The use of $PdH_{x/2}H_{x/2}$ implies that hydrogen atoms randomly distribute between the two sublattices for the TE structure. Note that if

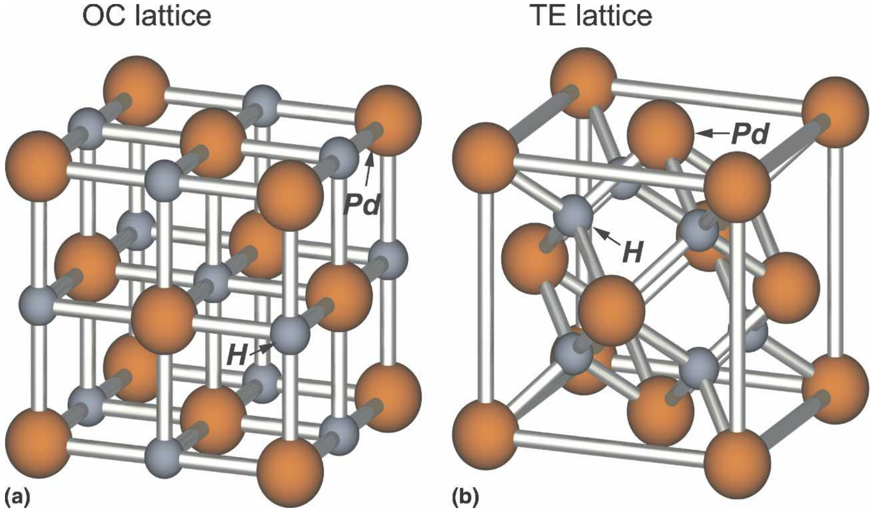

FIG. 1. Two PdH_x structures with (a) hydrogen at octahedral sites and (b) hydrogen at tetrahedral sites.

hydrogen atoms fully occupy one of the tetrahedral sublattice, it forms a zinc-blende PdH crystal, PdH_1H_0.

In a crystal, an atom interacts with its neighbors that appear at discrete distances. These neighbors can be grouped into neighbor shells (e.g., the nearest neighbor shell, the second neighbor shell, etc.). Assume that within the cutoff distance of the interaction, there are up to n neighbor shells. For convenience, we can view the lattice constant as uniquely determined by the lattice spacing, which is defined as the nearest neighbor distance in any of the fcc sublattices. Suppose that in a structure η (η = OC, TE), a central atom of species μ has $z_i(\eta, \mu, \nu)$ atoms in the ith neighbor shell of species ν. Obviously, z_i is a function of η, μ, and ν and can be predetermined. The corresponding relative distance to the ith neighbor shell is $\gamma_i(\eta, \mu, \nu)$, where the relative distance means that the distance $r_i(\eta, \mu, \nu)$ is scaled by the lattice spacing r_1, $\gamma_i(\eta, \mu, \nu) = r_i(\eta, \mu, \nu)/r_1$, so that γ_i is a predetermined structure parameter and is independent of the lattice constant. Here the lattice spacing can be represented by r_1 because by definition, it is independent of the structure η and species μ and ν. With these concepts, the cohesive energy of the η phase of the solid-solution Pd_yH_x can be written as

$$E_{c,\eta} = \frac{1}{(x+y)} \left\{ \begin{array}{l} y \cdot F_{Pd}(\rho_{Pd}) + x \cdot F_H(\rho_H) + \\ \dfrac{1}{2} \displaystyle\sum_{i=1}^{n_{Pd,Pd}} [y \cdot z_i(\eta,Pd,Pd) \cdot y \cdot \phi_{PdPd}(\gamma_i(\eta,Pd,Pd) \cdot r_1)] + \\ \dfrac{1}{2} \displaystyle\sum_{i=1}^{n_{H,H}} [x \cdot z_i(\eta,H,H) \cdot x \cdot \phi_{HH}(\gamma_i(\eta,H,H) \cdot r_1)] + \\ \displaystyle\sum_{i=1}^{n_{Pd,H}} [y \cdot z_i(\eta,Pd,H) \cdot x \cdot \phi_{PdH}(\gamma_i(\eta,Pd,H) \cdot r_1)] \quad , \end{array} \right. \tag{23}$$

where $n_{\mu,\nu}$ is the total number of ν neighbor shells surrounding a μ atom. The electron density at the atom μ site can be expressed as

$$\rho_\mu = \sum_{i=1}^{n_{\mu,Pd}} [z_i(\eta,\mu,Pd) \cdot y \cdot \rho^a_{Pd}(\gamma_i(\eta,\mu,Pd) \cdot r_1)] + \sum_{i=1}^{n_{\mu,H}} [z_i(\eta,\mu,H) \cdot x \cdot \rho^a_H(\gamma_i(\eta,\mu,H) \cdot r_1)] \quad . \tag{24}$$

With electron density defined by Eq. (24), Eq. (23) expresses the cohesive energy as a function of lattice spacing r_1 and fitting parameters. Because the expression does not require calculations for each atom, it can be calculated efficiently. During potential parameterization, the cohesive energy at the equilibrium lattice constant (or lattice spacing) can be conveniently achieved by optimizing the pressure to 0. Pressure can be calculated as

$$P = -\frac{\partial E_c}{\partial V} = -\frac{r_1}{3V} \frac{\partial E_c}{\partial r_1} \quad , \tag{25}$$

where V is volume per atom.

C. Bulk modulus *B* and elastic constants *C′* and C_{44}

Cubic crystals have three independent elastic constants C_{11}, C_{12}, and C_{44}. Alternatively, the three independent elastic constants can be represented by bulk modulus $B = (C_{11} + 2C_{12})/3$ and shear moduli $C' = (C_{11} - C_{12})/2$ and C_{44}. Our approach uses analytical equations in Mathematica to fit material properties. Analytical equations for elastic constants can be easily derived.

The bulk modulus is simply calculated using Eq. (23) as

$$B = V \frac{\partial^2 E_c}{\partial V^2} = \frac{r_1^2}{9V} \frac{\partial^2 E_c}{\partial r_1^2} \quad . \tag{26}$$

The elastic constant C_{ij} is defined as

$$C_{ij} = \frac{1}{V} \frac{\partial^2 E_c}{\partial \epsilon_i \partial \epsilon_j} \quad , \tag{27}$$

where ϵ_i and ϵ_j ($i, j = 1, 2, \ldots, 6$) are strains represented by the contracted notation.

To calculate the elastic constant C_{ij}, the cohesive energy needs to be expressed as a function of ϵ_i ($i = 1, 2, \ldots, 6$). Assuming that a lattice vector from atom i to atom j in an equilibrium crystal is represented by three components $\Delta x_{ij,0}$, $\Delta y_{ij,0}$, and $\Delta z_{ij,0}$, the three components become Δx_{ij}, Δy_{ij}, and Δz_{ij} after an $\epsilon_1, \epsilon_2, \ldots, \epsilon_6$ strain operation. This strain satisfies:

$$\begin{aligned} \Delta x_{ij} &= \Delta x_{ij,0} \cdot (1 + \epsilon_1) + 0.5 \cdot \Delta y_{ij,0} \cdot \epsilon_6 + 0.5 \cdot \Delta z_{ij,0} \cdot \epsilon_5 \\ \Delta y_{ij} &= 0.5 \cdot \Delta x_{ij,0} \cdot \epsilon_6 + \Delta y_{ij,0} \cdot (1 + \epsilon_2) + 0.5 \cdot \Delta z_{ij,0} \cdot \epsilon_4 \\ \Delta z_{ij} &= 0.5 \cdot \Delta x_{ij,0} \cdot \epsilon_5 + 0.5 \cdot \Delta y_{ij,0} \cdot \epsilon_4 + \Delta z_{ij,0} \cdot (1 + \epsilon_3) \quad . \end{aligned} \tag{28}$$

The distance between atoms i and j is

$$r_{ij} = (\Delta x_{ij}^2 + \Delta y_{ij}^2 + \Delta z_{ij}^2)^{1/2} \quad , \tag{29}$$

Substituting Eqs. (28) and (29) into Eqs. (1) and (2), the cohesive energy can be expressed as a function of strain and fitting parameters at the known lattice spacing. It should be noted that estimates of elastic constants must be made using lattice deformations during which atoms in the same neighboring shell may not always remain at the same distance to the center atom (except hydrostatic strain). As a result, Eqs. (1) and (2) instead of Eqs. (23) and (24) were used in Eq. (27) to calculate elastic constants.

VI. FITTING PROCEDURES

The goal is to fit the EAM potential to the desired lattice constant, heat of mixing, bulk modulus, and other elastic constants (C', C_{44}) of selected important structures as well as the relative energy difference between OC and TE phases. Four OC crystals $PdH_{0.250}$, $PdH_{0.500}$, $PdH_{0.750}$, and $PdH_{1.000}$, two TE crystals $PdH_{0.250}H_{0.250}$ and $PdH_{0.375}H_{0.375}$, and one fcc hydrogen crystal Pd_0H were considered. The desired properties of the TE structures were simply chosen to ensure that they are less stable than the corresponding (i.e., the same composition) OC structures. The desired properties of hydrogen were initially taken as the ones obtained from density function theory (DFT) calculations and then adjusted during the iterations of the fitting. The desired bulk modulus and elastic constants C' and C_{44} for the OC structures were taken from experiments.[41] The desired lattice constant and heat of mixing of the OC structures were integrated from both DFT calculations and experiments. First, the energy as a function of lattice spacing was determined from DFT calculations for the four OC structures $PdH_{0.250}$, $PdH_{0.500}$, $PdH_{0.750}$, and $PdH_{1.000}$. (These calculations were performed for the authors by Thomas K. Mattsson, a technical staff member of the High Energy Density Physics (HEDP) Theory department at Sandia National Laboratories, Albuquerque, NM.) As it is well known that cohesive energies determined from DFT calculations systematically deviate from experimental measurements, the DFT values were shifted to best match the experimental cohesive energies. The experimental cohesive energy of palladium element is known to be −3.91 eV. An experimental cohesive energy for the compound $PdH_{0.5}$ can be derived using the following reactions:

$$Pd_{(g)} \rightarrow Pd_{(s)} \quad , \tag{30}$$

$$Pd_{(s)} + \frac{1}{4} H_{2(g)} \rightarrow PdH_{0.5(s)} \quad , \tag{31}$$

and

$$\frac{1}{2} H_{(g)} \rightarrow \frac{1}{4} H_{2(g)} \quad . \tag{32}$$

Here the subscripts (s) and (g) represent solid and gas states of the materials, respectively. The energy change of Eq. (30) is equivalent to the palladium cohesive energy.[32] The energy changes of Eqs. (31) and (32) have been measured experimentally.[42,43] By summing Eqs. (30), (31), and (32), an experimental cohesive energy of the $PdH_{0.5}$ compound was determined as −3.4877 eV/atom. The two experimental cohesive energies for Pd and $PdH_{0.5}$ allow us to determine the respective energy shifts per palladium and per hydrogen atom. These in turn allow us to adjust the cohesive energy of a structure based on its composition. The adjusted cohesive energies, along with the lattice constants, are shown in Table I for the five important OC structures.

The adjustments of DFT cohesive energies discussed previously also connect to the much larger issue of quantum mechanical effects on the motion and energy of hydrogen atoms. Recent work by Caputo and Alavi[44] shows that the use of DFT incorrectly predicts tetrahedral site occupancy and a zinc-blende structure for significant amounts of H ($x = 0.25$ to 1) in the Pd–H alloy system. They hypothesize that DFT omits vibrational zero-point energy (ZPE), and that inclusion of ZPE is responsible for the octahedral occupancy observed in experimental systems. This quantum effect is significant for light elements such as hydrogen, whereas the additional amount of ZPE neglected may not be as significant for heavier elements that act as interstitial impurities. Clearly, further investigation of this issue, and other quantum mechanical effects, is warranted.

An objective function was defined as a weighted sum of the square deviation of predicted properties from the target properties for all the structures being fitted. These properties include the heat of mixing, relative energy difference, pressure, bulk modulus, and elastic constants C' and C_{44}. The target values for the pressure are set to 0 to enforce equilibrium lattice constants. Some properties, such as those of the TE structures, do not require an exact match. We then use options “>” or “<” instead of “=.” Only when the predicted properties violate these options when compared with their target values will the corresponding square deviation be summed into the objective function.

It is important to implement a cutoff distance r_c for both atomic electron density and pair energy functions. Two steps are used. First, we need to ensure that both functions naturally (i.e., by themselves) decay to small values when r gets close to r_c, say, $r = r_c - r_s$, where r_s is a small distance. This can be achieved by using the constraints

$$\phi(r_c - r_s)/\phi(r_{1,e}) < \epsilon \quad , \tag{33}$$

and

$$\rho^a(r_c - r_s)/\rho^a(r_{1,e}) < \epsilon \quad , \tag{34}$$

during optimization, where ϵ is a small number, and $r_{1,e}$ is the equilibrium lattice spacing of the equilibrium structure (a nominal atomic separation that is highly likely to be seen during simulations). The second step is to ensure

TABLE I. Adjusted DFT properties.

Properties/structures	$PdH_{0.000}$	$PdH_{0.250}$	$PdH_{0.500}$	$PdH_{0.750}$	$PdH_{1.000}$
Lattice constant a (Å)	3.960	4.020	4.077	4.109	4.147
Cohesive energy E_c (eV/atom)	−3.910	−3.647	−3.488	−3.363	−3.261

that both pairwise functions indeed drop to zero at $r = r_c$. This can be done by multiplying them with a cutoff function $(1 + \cos[\pi(r - r_c + r_s)/r_s])/2$ when $r > r_c - r_s$.

With proper bounds for all parameters, optimization is done using four Mathematica[45] built-in methods: differential evolution, simulated annealing, default, and Nelder Mead algorithm. The use of four different methods increases the probability of finding a global minimum as the four methods usually produce different results (unless the initial parameters that are used for all methods are already close to the global minimum point). Iterative fitting is carried out by varying fitting conditions (e.g., cutoff distances, weights, target values, constraints, use of ">" or "<" fitting options instead of "=" option or vice versa, etc.) until satisfactory results are obtained. The fitted parameters obtained through this process are listed in Table II. The potentials give $F'_{\mathrm{Pd,u}}(\rho_{0,\mathrm{Pd}}) = 0.251546$, and $F'_{\mathrm{H,u}}(\rho_{0,\mathrm{H}}) = -0.0296604$. Here, a value of $\rho_{0,\mathrm{H}} = 7.98909$ was determined by using Eqs. (2) and (8) and assuming a fcc H crystal structure at a target value of lattice constant 3.38 Å.

VII. CHARACTERISTICS OF THE POTENTIAL

A. EAM functions

To characterize the fitted potential, we first examine all the normalized EAM functions in Fig. 2. Here, $F_{\mathrm{Pd}}(\rho)$,$\rho^a_{\mathrm{Pd}}(r)$, and $\phi_{\mathrm{PdPd}}(r)$ were calculated from Eqs. (5), (A2), and (6), respectively, $F_{\mathrm{H}}(\rho)$,$\rho^a_{\mathrm{H}}(r)$, and $\phi_{\mathrm{HH}}(r)$ were calculated from Eqs. (10), (8), and (7), respectively, and $\phi_{\mathrm{PdH}}(r)$ was calculated from Eq. (14). The $F_{\mathrm{Pd,u}}(\rho)$, $\phi_{\mathrm{PdPd,u}}(r)$, and $F_{\mathrm{H,u}}(\rho)$ required for the calculations are defined by Eqs. (A1), (A3), and (9). Radial functions $\rho^a_{\mathrm{H}}(r)$, $\phi_{\mathrm{HH}}(r)$, and $\phi_{\mathrm{PdH}}(r)$ were cutoff using the cutoff function described previously. Smooth curves can be seen for all the functions in Fig. 2. Due to the application of the two normalization approaches, Fig. 2(a) shows well-behaved embedding energy functions for palladium and hydrogen that reach a minimum at comparable electron densities. The Pd–Pd and H–H pair energies shown in Fig. 2(c) reach a minimum at the atomic spacings that are proportional to their lattice constants. The magnitudes of the pair energies are also comparable. The equilibrium separation of the Pd–H pair energy is shorter, and the corresponding binding energy is higher. Finally, the decay of the electron density functions shown in Fig. 2(b) appears reasonable and similar for both palladium and hydrogen over the atomic separation distance range commonly encountered in simulations [i.e., ⩾2 Å for palladium and ⩾1.5 Å for hydrogen, see Fig. 2(c)].

TABLE II. EAM parameters.

Embedding energy (eV)				
i	c_i	d_i	a_i	b_i
H	0.000197047	1.18860	9.99780	60.0155
Electron density				
i	C_i	δ_i	$\rho_{0,i}$	⋯
H	11.0025	1.30927	7.98909	⋯
Pair energy (eV)				
ij	D_{ij}	α_{ij}	β_{ij}	$r_{0,ij}$
PdH	0.2494540	4.82613	2.13158	1.50964
HH	0.0661496	3.67263	1.47797	2.51980
Cutoff radii (Å)				
ij	$r_{c,ij}$	$r_{s,ij}$	⋯	⋯
PdH	4.9500000	0.30000	⋯	⋯
HH	5.3500000	0.30000	⋯	⋯

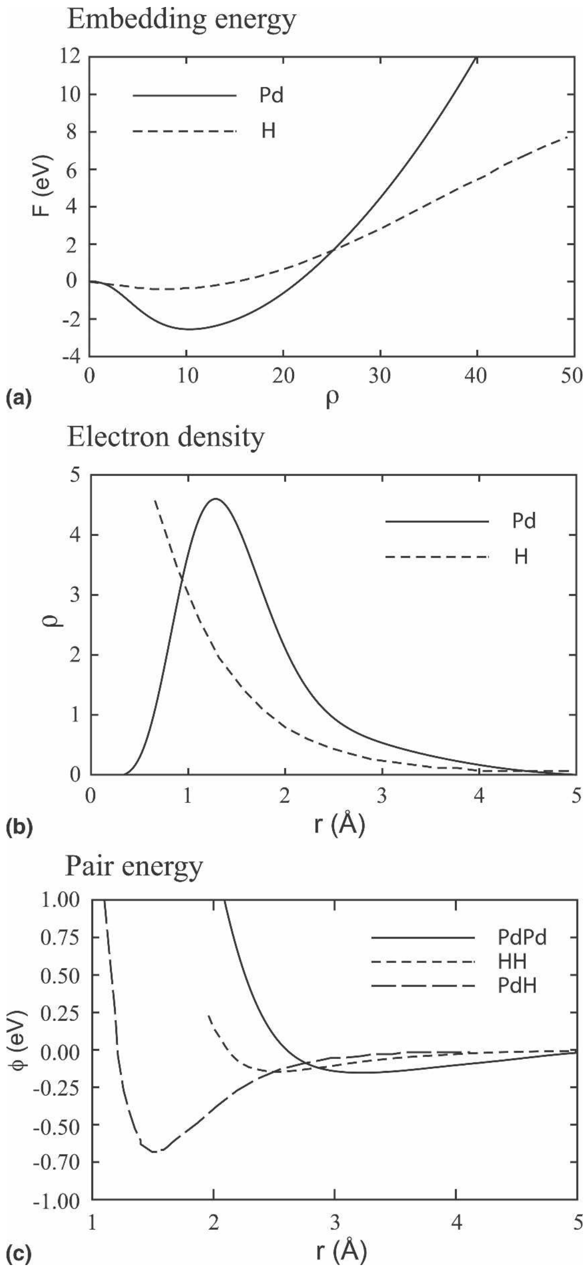

FIG. 2. EAM function curves for (a) embedding energy [as defined in Eqs. (5), (A1), (9), and (10)], (b) electron density [as defined in Eqs. (A2) and (8)], and (c) pair energy [as defined in Eqs. (6), (A2), (A3), (7), and (14)].

Based on this potential, molecular statics simulations were used to minimize the energy of various OC structures as a function of composition using a cubic computational system containing 6 × 6 × 6 fcc unit cells (corresponding to 864 palladium atoms) or more. The resulting crystals were used to evaluate the lattice constant, cohesive energy, and elastic constants C_{11}, C_{12}, and C_{44}, and the results are shown in Table III. It should be noted that the palladium elastic constants listed in Table III are slightly different from the values in Ref. 32. This is because the tabular palladium potential functions[32] do not have smooth second derivatives, and we have approximated them with the high-order polynomial functions, shown in the Appendix. Our polynomial functions have almost the same values and the same first derivatives to the original tabular functions, but have slightly different second derivatives. This causes differences in elastic constant predictions, but not the cohesive energy or the lattice constant.

B. Energy as a function of lattice spacing

We further explore the behavior of the potential on predicting the system energy as the crystal is compressed or stretched. The energy per atom as a function of lattice spacing is plotted in Fig. 3 for two representative phases, $PdH_{0.250}$ and $PdH_{0.500}$. Again, smooth curves are seen in Fig. 3. It can be seen that as the hydrogen composition increases, the lattice constant increases, and the magnitude of cohesive energy becomes lower, in good agreement with the trend shown in Table III.

C. Equilibrium lattice spacing

The equilibrium lattice constant as a function of composition is an important property as it causes stress when adjacent regions have different compositions or even different phases. To characterize the fitted potential, the predicted equilibrium lattice spacing as a function of composition is shown as solid circles in Fig. 4 for the OC PdH_x structure. For comparison, the DFT data are shown as open circles, and the experimental values[46] are shown as the short dashed line. To guide the eye, solid and long dashed lines are used to connect the data points. It can be seen that the trend of an increasing equilibrium lattice spacing with increasing hydrogen composition is predicted by our potential. The predicted equilibrium lattice spacing lies between experimental and DFT calculated values at small compositions, but is larger than both experimental and DFT calculated values at larger compositions. This difference arose as a trade-off to better fit the phase miscibility gap.

TABLE III. Predicted values of lattice constant a, cohesive energy E_c, and elastic constants C_{11}, C_{12}, and C_{44}.

Structures	a (Å)	E_c (eV/atom)	C_{11} (GPa)	C_{12} (GPa)	C_{44} (GPa)
$PdH_{0.000}$	3.885	−3.910	245.8	199.8	54.7
$PdH_{0.087}$	3.923	−3.770	226.0	186.5	44.7
$PdH_{0.185}$	3.965	−3.638	207.7	173.4	38.9
$PdH_{0.292}$	4.010	−3.520	194.1	162.7	32.7
$PdH_{0.378}$	4.045	−3.439	186.0	156.2	28.9
$PdH_{0.476}$	4.083	−3.361	181.4	152.0	26.7
$PdH_{0.558}$	4.113	−3.303	183.9	152.5	27.5
$PdH_{0.666}$	4.148	−3.238	208.3	163.1	33.5
$PdH_{0.784}$	4.180	−3.176	241.5	176.7	36.4
$PdH_{0.885}$	4.202	−3.129	245.9	181.9	33.2
$PdH_{1.000}$	4.225	−3.081	241.7	190.3	25.5

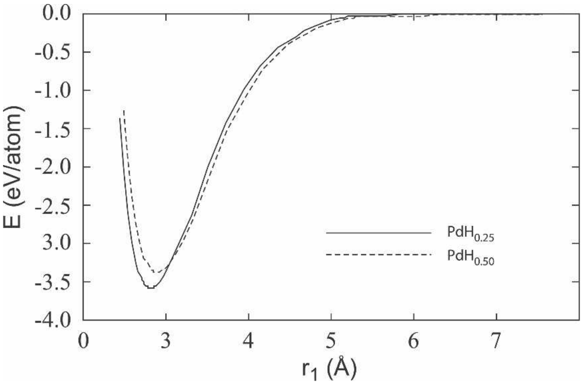

FIG. 3. Energy as a function of lattice spacing for OC lattices.

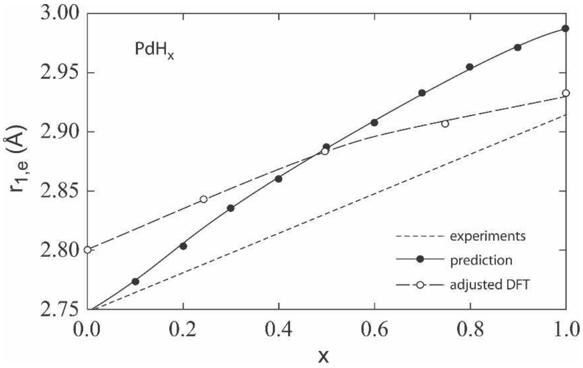

FIG. 4. Lattice spacing as a function of composition for OC lattices.

D. Cohesive energy

The shape of the cohesive energy as a function of hydrogen composition relates directly to the phase miscibility gap. In addition, the equilibrium OC structures must have lower cohesive energies than the TE structures over the entire composition range. Predicted cohesive energies as functions of composition x are shown in Fig. 5 using the filled circles for the TE structure and the open circles for the OC structure. Here cohesive energies of the OC structure were the minimum energy obtained from molecular statics simulations, listed in Table III. The same approach cannot be used for unstable TE structures as they will transform to OC structures in simulations. As a result, the cohesive energies of the TE

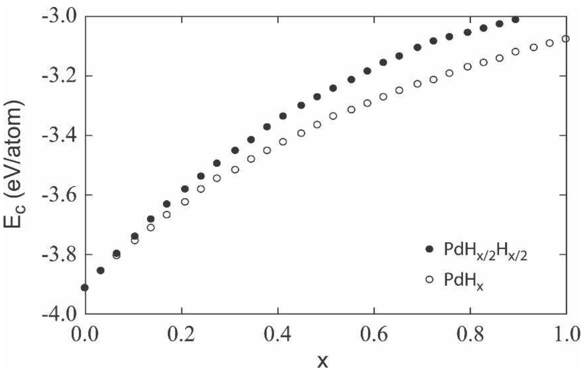

FIG. 5. Cohesive energy as a function of composition for OC and TE lattices.

structure were calculated using Eq. (23) at the equilibrium lattice spacing $r_{1,e}$. It can be seen from Fig. 5 that the potential correctly predicts a more stable OC structure than a TE structure over the entire composition range $0 \leqslant x \leqslant 1$.

The quantity shown in Fig. 5 is energy per atom. As $x \to 0$, the solution becomes infinitely dilute and the number of palladium atoms becomes infinitely large compared with that of the hydrogen atoms. As a result, values of energy per atom for both OC and TE structures converge to the palladium cohesive energy. Figure 5, therefore, does not sensitively show the relative stability of OC and TE structures at small compositions. Relaxed total energies were hence calculated using a large fcc palladium crystal with a single hydrogen atom placed at OC and TE sites. We found that the total energy with the hydrogen atom at the TE site is about 0.127 eV higher than that with the hydrogen atom at the OC site.

E. Gibbs free energy of mixing

To verify the existence of the phase miscibility gap and to estimate the compositions of the α and β phases when they are in equilibrium, the cohesive energy data obtained from molecular statics simulations were used in Eq. (15) to calculate the Gibbs free energy of mixing as a function of mol fraction for the OC structure. The results are plotted in Fig. 6 at two temperatures, 300 and 500 K. Figure 6 clearly shows that the system splits into two coexisting phases. At the low temperature of 300 K, the equilibrium mole fractions for the α and β phases are $X = 0$ and 0.45, respectively, corresponding to x of 0 and (approximately) 0.82. While the potential correctly predicts the phase separation, the equilibrium composition for the α and β phases are somewhat underestimated and overestimated, respectively. As mentioned previously, it has been experimentally determined that phase boundaries at room temperature are $x = 0.03$ and 0.6.[18] It should be noted that such a discrepancy was also characteristic of the "lost" potential by Wolf et al.[25] They noted α and β compositions of $x = 0.1385$ and 0.8362.

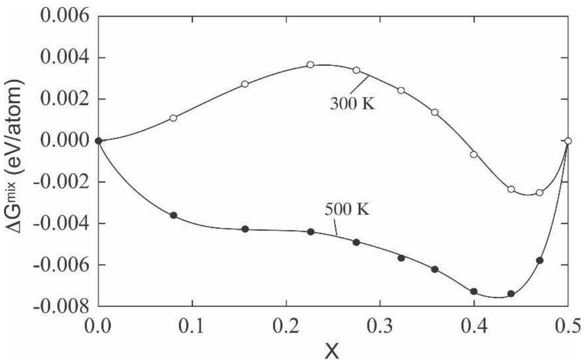

FIG. 6. Gibbs free energy of mixing as a function of mol fraction for the OC structure.

Our potential is an improvement in this regard. At the high temperature of 500 K, the mol fractions for the α and β phases become closer to $X = 0.1$ and 0.4, respectively, corresponding to x of about 0.11 and 0.67.

F. Elastic constants

The minimized energy OC configurations were used to calculate the elastic constants B, C', and C_{44}, converted from the values for C_{11}, C_{12}, and C_{44} listed in Table III. The results are shown in Fig. 7 as functions of composition.

It can be seen that the general trend of how elastic constants vary with composition matches well with the experiments by Schwarz et al.[41] Also, the quantitative agreement is very good, especially considering that these experimental values were only weakly used in the fitting process. Several specific features can be noticed: The value of the bulk modulus at high concentrations of hydrogen, i.e., beyond the β phase boundary composition, is only slightly lower than the value at the dilute limit, and is essentially flat within the high concentration range $0.82 \leqslant x \leqslant 1$. C', shown in Fig. 7(b), exhibits a peak value at the equilibrium composition of the β phase. Our computationally determined curve even has a shape similar to the one theorized by Schwarz et al. and shown in Fig. 9 of their paper.[41] The value of C_{44}, while differing somewhat from the bilinear form supposed by Schwarz et al., does show a decreasing trend over the high hydrogen concentration range of $0.82 \leqslant x \leqslant 1$. Also, it does appear that a line connecting the β concentration point with the $x = 0$ (pure palladium) point would have a lower slope than a line interpolated through the high concentration points.

G. Mechanical strength

We also performed molecular statics calculations to explore the mechanical behavior of the PdH_x OC structure as a function of composition. We first examined the tensile strength using systems containing 6 × 6 × 6 cubic

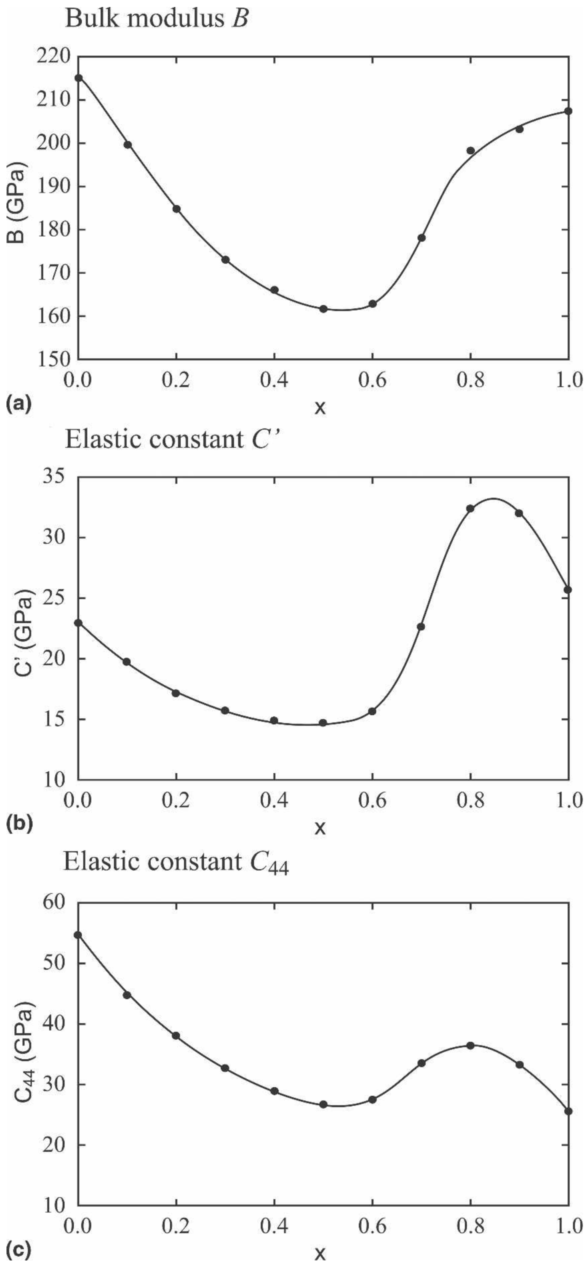

FIG. 7. Elastic constants as a function of composition for OC structure. (a) B. (b) C'. (c) C_{44}. Curved, solid lines are shown as guides for connecting the simulated data.

cells in the three coordinate directions (a total of 864 to 1728 atoms depending on the hydrogen concentration). Periodic boundary conditions were used in all directions, and the system was sequentially stretched in the y-direction by a strain increment of 0.00005. For each stretch increment, the energy of the system was minimized and a constant zero pressure condition was applied in the x- and z-directions to simulate uniaxial stress loading. The virial stress of the relaxed system as a function of stretch was calculated. Two examples, $PdH_{0.1}$ and $PdH_{0.8}$, respectively, are shown in Fig. 8.

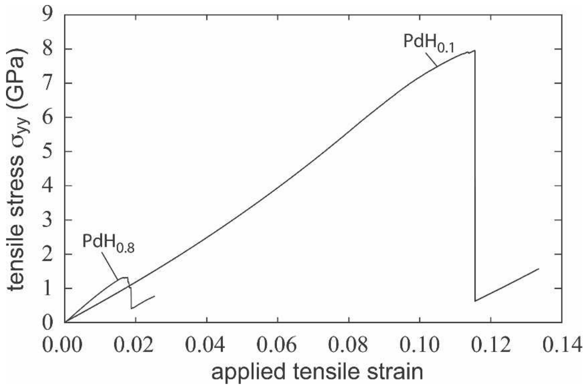

FIG. 8. Tensile stress as a function of stretch.

In Fig. 8, the applied tensile strain is defined as $\epsilon = (1.00005)^n - 1$ where n is the number of stretch increments applied. If strength is defined as the maximum stress in the stress versus applied tensile strain curve, the results in Fig. 8 indicate that the strength of the material decreases with increasing hydrogen composition. This is indeed shown to be the case in Fig. 9, where strength is plotted as a function of composition. Our results indicate that tensile strength decreases monotonically as hydrogen composition is increased.

We next examined shear strength, using systems containing 10 × 10 × 10 cubic cells for a total of 4000 to 8000 atoms. Periodic boundary conditions are applied in the x- and z-directions, while the top and bottom layers (referred to the y-direction) are displaced in the x-direction to simulate a simple shear mode of deformation. As the shear is applied, the system is allowed to relax in the y-direction, but the x- and z- dimensions are kept constant. A strain increment of 0.0001 is used. Due to the nonperiodicity of the boundaries in the y-direction, the stress is not calculated using all the atoms within the system. Rather, a subregion in the middle of the system with a dimension of 10 × 5 × 10 cubic cells is used to estimate the stresses, thereby minimizing the effect of boundary conditions on this material property. Figure 10

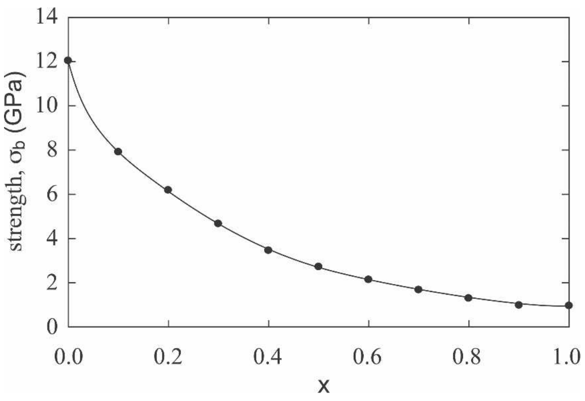

FIG. 9. Tensile strength as a function of composition for OC structures.

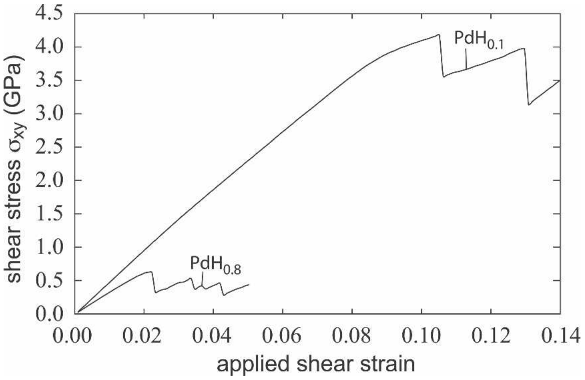

FIG. 10. Shear stress as a function of applied strain.

shows how this estimate of shear stress varies with the applied shear strain, and Fig. 11 shows how shear strength, the maximum value for these shear stress curves, varies as a function of composition. It is observed that for our potential, shear strength also decreases with increasing hydrogen concentration.

VIII. MOLECULAR DYNAMICS SIMULATIONS

The simulations discussed previously were all carried out under static conditions and relaxed atomic spacing. During MD simulations, atoms are disturbed from their ideal lattice sites. This allows the system to sample many of the configurations that have not been sampled under the static conditions. As a result, statically stable structures may become unstable during MD simulations. We have therefore carried out a series of MD simulations to verify the fidelity of our potential.

In the first type of simulations, OC and TE structures with various compositions were annealed for a nanosecond at various temperatures ranging from 200 to 500 K using the MD simulation approach. All OC structures were found stable, and all TE structures were found to transform to OC structures. As an example, an initial $PdH_{0.392}H_{0.392}$ TE structure containing 6 × 6 × 6 cubic cells in the three coordinate directions is shown in Fig. 12(a). Molecular dynamics was first used to anneal the structure at 300 K for a nanosecond. Molecular statics was subsequently used to minimize the energy of the system. The atomic configuration after MD + MS simulations is shown in Fig. 12(b). It can be seen that many of the hydrogen atoms switched from the tetrahedral sites to the octahedral sites during the MD + MS energy minimization process. The potential hence ensures both phase stability and the correct hydrogen interstitial sites.

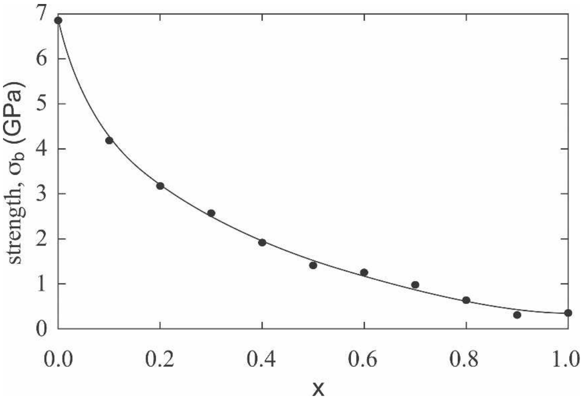

FIG. 11. Shear strength as a function of composition for OC structures.

The second type of MD tests used the same crystal geometry to examine the diffusion of a single hydrogen atom. We found that when the velocities for all atoms in the system were initialized according to a Boltzmann energy distribution consistent with the initial system temperature, classical MD simulation always predicted a hydrogen atom jump rate that was almost the same as its vibrational rate. This occurred in both constant energy and constant temperature simulations that were carried out using time steps ranging from 0.00005 to 0.001 ps (small time steps were needed because the hydrogen atom moved very fast as its mass is about 100 times smaller than that of a palladium atom). To correct for this, we discovered that if the initial system temperature is used to initialize velocities for only the palladium atoms while the hydrogen velocities were set to 0, or the mass of hydrogen atom was artificially increased to a value comparable to that of a palladium atom, then realistic diffusion jump rates were obtained.

Because the hydrogen mass was small, little energy transfer occurred during each vibration of the hydrogen atom in the palladium lattice. If the hydrogen acquired enough energy (either due to velocity initialization or the dragging force used for constant temperature simulation) that could overcome the energy barrier for jumps, it maintained its jump capability over a long time, resulting in fast jump rates. It is not clear if the temperature initialization or the temperature control routines used in classical MD simulations are accurate representations of the equilibrium atomistic systems involving particles with vastly different masses. We believe that a realistic simulation requires a constant energy MD simulation over a long time using a very small time step with a zero initial velocity for the hydrogen atom. Since our purpose was to test the potential, a more efficient computational approach was used. We artificially increased the mass of the hydrogen atom to that of a palladium atom. This increase will change the vibrational frequency (for harmonic systems, vibration frequency is inversely proportional to the square root of the mass), but not the activation energy barrier for the jumps. The time evolution of the position of the hydrogen atom obtained from a MD simulation at a temperature of 300 K is shown in Fig. 13. A hydrogen atom was initially put at an octahedral site Fig. 13(a). After 440 ps, the hydrogen was seen to make a first jump to a tetrahedral site, Fig. 13(b). After an

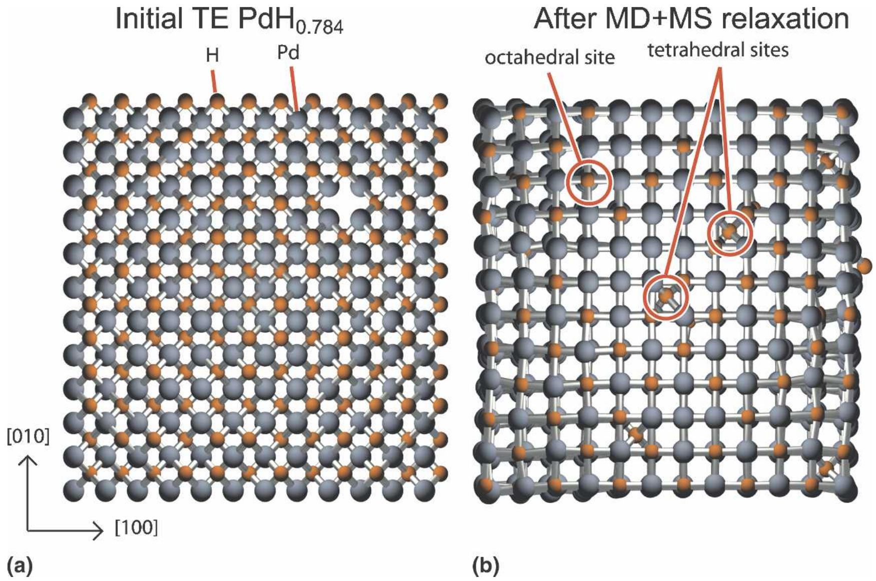

FIG. 12. Change of atomic configurations of a $PdH_{0.784}$ phase due to MD annealing at 300 K for 1 ns followed by MS energy minimization. (a) The TE structure before MD + MS relaxation and (b) after MD + MS energy relaxation.

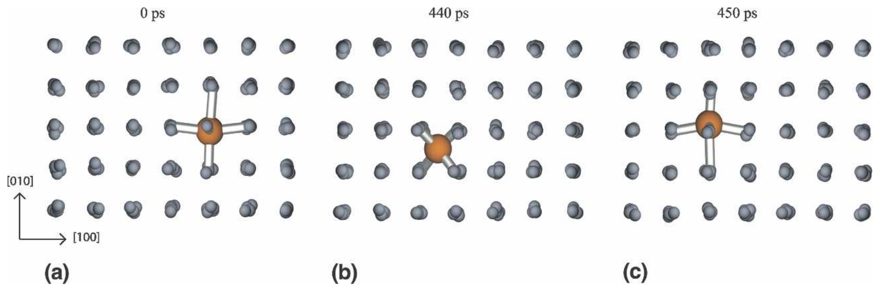

FIG. 13. Snapshots of single hydrogen atom diffusion in a palladium matrix. Time: (a) 0 ps, (b) 440 ps, and (c) 450 ps. The size of the hydrogen atom is magnified for clarity.

additional 10 ps, the hydrogen atom was again seen to jump to an octahedral site, Fig. 13(c). As a result, jumps occur on the order of 400 ps, via an octahedral → tetrahedral → octahedral path. The fast diffusion is in good agreement with experiments.[47]

As already noted, our mass change for hydrogen atoms affects the vibration frequencies observed but not the energy barriers present due to the potential energy landscape. However, mass and energy are not the only characteristics that affect jumping mechanisms. Contributions from entropy, specifically the migration entropy, also play a role. It is therefore possible that our approach modifies the jumping mechanisms observed. We emphasize that the results presented here only serve as a means to characterize our potential. Those intent on the accurate simulation of diffusion mechanisms are encouraged to explore these issues.

IX. CONCLUSIONS

Analytical EAM potentials have been developed and integrated with a published EAM potential of palladium to form a Pd–H alloy EAM potential. This potential is suitable for any composition of the Pd–H system. It well predicts the lattice constant, cohesive energy, bulk modulus, and other elastic constants for a variety of structures. It can also predict the phase miscibility gap for the Pd–H system. Direct MD simulations indicate that this potential ensures the phase stability during dynamic simulations and can correctly capture the diffusion mechanism of hydrogen in the palladium lattice. The following approaches were found to be critical to the development:

(1) hydrogen and other nonequilibrium phases must be included in the potential parameterization;

(2) both the embedding energy and electron density functions must be normalized for palladium and hydrogen to create a well-behaved alloy potential;

(3) a solid-solution model significantly improves the efficiency of the potential parameterization while still possesses sufficient accuracy needed for the potential;

(4) more general embedding and pair energy functions can be used to improve the fitting; and

(5) the parameterization must be carried out iteratively with respect to cutoff distance, adjustment of target

values, the weights used to define the objective function, the bounds for parameters or other constraints, and fitting options such as “>” or “<” instead of “ = .”

ACKNOWLEDGMENTS

The authors gratefully acknowledge input provided by discussions with M.I. Baskes, D.F. Cowgill, S.M. Foiles, J. Griffin, C.D. Lorenz, M.G. Martin, T.K. Mattsson, S.L. Robinson, R.B. Schwarz, C.S. Snow, G.C. Story, and R.T. Walters. Sandia is a multiprogram laboratory operated by Sandia Corporation, a Lockheed Martin Company, for the United States Department of Energy’s National Nuclear Security Administration under Contract DE-AC04-94AL85000.

REFERENCES

1. R. Lasser: *Tritium and Helium-3 in Metals,* Vol. 9 (Springer-Verlag, Berlin, 1989).
2. *Hydrogen in Metals,* edited by G. Alefeld and J. Völkl, Vol. 1 (Springer-Verlag, Berlin, 1978).
3. *Hydrogen in Metals,* edited by G. Alefeld and J. Völkl, Vol. 2 (Springer-Verlag, Berlin, 1978).
4. *Transition Metal Hydrides,* edited by E.L. Muetterties (Marcel Dekker, New York, 1971).
5. W.M. Mueller, J.P. Blackledge, and G.G. Libowitz: *Metal Hydrides* (Academic Press, New York, 1968).
6. Y. Fukai: *The Metal-Hydrogen System,* Vol. 21 (Springer-Verlag, Berlin, 1993).
7. R. Povel, K. Feucht, W. Gelse, and G. Withalm: Hydrogen fuel for motorcars. *Interdiscip. Sci. Rev.* **14**(4), 365 (1989).
8. M.S. Ortman, L.K. Heung, A. Nobile, and R.L. Rabun: Tritium processing at the Savannah River site—Present and future. *J. Vac. Sci. Technol., A* **8**(3), 2881 (1990).
9. L.K. Heung: Heat transfer and kinetics of a metal hydride reactor. *Z. Phys. Chem. Neue Folge* **164,** 1415 (1989).
10. M.S. Ortman, T.J. Warren, and D.J. Smith: Use of metal hydrides for handling tritium. *Fusion Technol.* **8**(2), 2330 (1985).
11. V.I. Anisimkin, I.M. Kotelyanskii, P. Verardi, and E. Verona: Elastic properties of thin film palladium for surface-acoustic-wave (SAW) sensors. *Sens. Actuators, B* **23**(2–3), 203 (1995).
12. L.A. Nygren and R.G. Leisure: Elastic constants of α'-Phase PdH_x over the temperature range 4–300 K. *Phys. Rev. B* **37**(11), 6482 (1988).
13. D.K. Hsu and R.G. Leisure: Elastic constants of palladium and β-phase palladium hydride between 4 and 300 K. *Phys. Rev. B* **20**(4), 1339 (1979).
14. A.A. Lucas: Helium in metals. *Phys. B + C (Amsterdam).* **127**(1–3), 225 (1984).
15. S. Thiebaut, B. Decamps, J.M. Penisson, B. Limacher, and A.P. Guegan: TEM study of the aging of palladium-based alloys during tritium storage. *J. Nucl. Mater.* **277**(2–3), 217 (2000).
16. C. Cawthorne and E.J. Fulton: Voids in irradiated stainless steel. *Nature* **216**(5115), 575 (1967).
17. G.C. Abell and A. Attalla: NMR studies of aging effects in palladium tritide. *Fusion Technol.* **14**(2), 643 (1988).
18. S.H. Goods and S.E. Guthrie: Mechanical properties of palladium and palladium hydride. *Scripta Metall. Mater.* **26,** 561 (1992).
19. R.T. Walters and M.W. Lee: 2 plateaus for palladium hydride and the effect of helium from tritium decay on the desorption plateau pressure for palladium tritide. *Mater. Char.* **27**(3), 157 (1991).
20. G. Andreasen, A. Visintin, R.C. Salvarezza, W.E. Triaca, and A.J. Arvia: Hydrogen induced deformation of metals followed by in situ scanning tunneling microscopy, palladium electrolytic hydrogen charging and discharging in alkaline solution. *Langmuir* **15**(1), 1 (1999).
21. M.S. Daw and M.I. Baskes: Embedded atom method—Derivation and application to impurities, surfaces, and other defects in metals. *Phys. Rev. B* **29**(12), 6443 (1984).
22. M.S. Daw and M.I. Baskes: Semiempirical quantum mechanical calculations of hydrogen embrittlement in metals. *Phys. Rev. Lett.* **50**(17), 1285 (1983).
23. S.M. Foiles, M.I. Baskes, and M.S. Daw: Embedded atom method functions for the fcc metals Cu, Ag, Au, Ni, Pd, Pt, and their alloys. *Phys. Rev. B* **33**(12), 7983 (1986).
24. W. Zhong, Y.S. Li, and D. Tomanek: Effect of adsorbates on surface phonon modes—H on Pd(001) and Pd(110). *Phys. Rev. B* **44**(23), 13053 (1991).
25. R.J. Wolf, M.W. Lee, R.C. Davis, P.J. Fay, and J.R. Ray: Pressure–composition isotherms for palladium hydride. *Phys. Rev. B* **48**(17), 12415 (1993).
26. R.J. Wolf, K.A. Mansour, M.W. Lee, and J.R. Ray: Temperature dependence of elastic constants of embedded-atom models of palladium. *Phys. Rev. B* **46**(13), 8027 (1992).
27. R.J. Wolf, P.J. Fay, and J.R. Ray (private communication, 2002).
28. X.W. Zhou, H.N.G. Wadley, R.A. Johnson, D.J. Larson, N. Tabat, A. Cerezo, A.K. Petford-Long, G.D.W. Smith, P.H. Clifton, R.L. Martens, and T.F. Kelly: Atomic scale structure of sputtered metal multilayers. *Acta Mater.* **49**(19), 4005 (2001).
29. W. Zou, H.N.G. Wadley, X.W. Zhou, R.A. Johnson, and D. Brownell: Surfactant mediated growth of giant magnetoresistance multilayers. *Phys. Rev. B* **64**(17), 174418 (2001).
30. M. Ruda, D. Farkas, and J. Abriata: Embedded atom interatomic potentials for hydrogen in metals and intermetallic alloys. *Phys. Rev. B* **54**(14), 9765 (1996).
31. X.W. Zhou, R.A. Johnson, and H.N.G. Wadley: Misfit energy increasing dislocations in vapor deposited CoFe/NiFe multilayers. *Phys. Rev. B* **69**(14), 144113 (2004).
32. S.M. Foiles and J.J. Hoyt: *Computer Simulation of Bubble Growth in Metals Due to He* (Sandia National Laboratories, 2001).
33. J.H. Rose, J.R. Smith, F. Guinea, and J. Ferrante: Universal features of the equation of state of metals. *Phys. Rev. B* **29**(6), 2963 (1984).
34. J.A. Zimmerman: *Computer Simulation of Boundary Effects on Bubble Growth in Metals Due to He* (Sandia National Laboratories, 2003).
35. ParaDyn, 2007, available online at http://www.cs.sandia.gov/~sjplimp/.
36. R.A. Johnson: Alloy models with the embedded atom method. *Phys. Rev. B* **39**(17), 12554 (1989).
37. S.M. Foiles: Application of the embedded atom method to liquid transition metals. *Phys. Rev. B* **32**(6), 3409 (1985).
38. M.W. Finnis and J.E. Sinclair: A simple empirical N body potential for transition metals. *Philos. Mag. A* **50**(1), 45 (1984).
39. A. Prince: *Alloy Phase Equilibria* (Elsevier Publishing Co., Amsterdam, 1966).
40. A.S. Richard: *Thermodynamics of Solids* (John Wiley & Sons, New York, 1972).
41. R.B. Schwarz, H.T. Bach, U. Harms, and D. Tuggle: Elastic properties of Pd–hydrogen, Pd–deuterium, and Pd–tritium single crystals. *Acta Mater.* **53**(3), 569 (2005).
42. International Critical Tables of Numerical Data, *Physics, Chemistry and Technology,* 1st ed. National Research Council, edited by E.W. Washburn and C.J. West, Vol. 7 (McGraw-Hill Book Co., New York, 1930).
43. *CRC Handbook of Chemistry and Physics* (CRC Press, Cleveland, OH, 1977).

44. R. Caputo and A. Alavi: Where do the H atoms reside in PdH$_x$ systems? *Mol. Phys.* **101**(11), 1781 (2003).
45. Wolfram Research Inc., 2007, available online at: http://www.wolfram.com/products/mathematica/index.html.
46. Y. Sakamoto, K. Yuwasa, and K. Hirayama: X-ray investigation of the absorption of hydrogen by several palladium and nickel solid solution alloys. *J. Less-Comm. Metals* **88,** 115 (1982).
47. Y. Fukai and H. Sugimoto: Diffusion of hydrogen in metals. *Adv. Phys.* **34**(2), 263 (1985).

APPENDIX: HIGH-ORDER POLYNOMIAL PALLADIUM EAM FUNCTIONS

For easy use within our potential fitting program, the palladium EAM functions have been converted to high-order polynomial functions:

$$\begin{aligned}
F_{\mathrm{Pd,u}}(\rho) &= 295{,}878.9003038662\cdot(\hat{\rho} - 0.20581955357385892)\\
&\cdot(\hat{\rho} - 0.081228755904399)\cdot\hat{\rho}\cdot(\hat{\rho} + 0.05298811034615951)\\
&\cdot[\hat{\rho}\cdot(\hat{\rho} - 2.4242616904962846) + 1.4791899886249564]\\
&\cdot[\hat{\rho}\cdot(\hat{\rho} - 2.1376274623740064) + 1.2169215689822592]\\
&\cdot[\hat{\rho}\cdot(\hat{\rho} - 1.6486007989726832) + 0.8159825255339774]\\
&\cdot[\hat{\rho}\cdot(\hat{\rho} - 1.0749204110338482) + 0.42007491336688396]\\
&\cdot[\hat{\rho}\cdot(\hat{\rho} - 0.5128056047933808) + 0.12468685331167456]
\end{aligned} \tag{A1}$$

where $\hat{\rho} \equiv \rho/50$.

$$\rho^{\mathrm{a}}_{\mathrm{Pd}}(r) = -0.02972698211669922 + \hat{r}\cdot\left\{\begin{array}{l} 0.6676807403564453 + \\ \hat{r}\cdot\left[\begin{array}{l} -255.8965835571289 + \hat{r}\cdot \\ (14{,}673.409149169922 \\ -(2.597301181336601\times 10^{7})\rho_{\mathrm{a}}(r)) \end{array}\right] \end{array}\right\} , \tag{A2}$$

where

$$\begin{aligned}
\rho_{\mathrm{a}}(r) &= \hat{r}\\
&\cdot[\hat{r}\cdot(\hat{r} - 2.7267629107325706) + 1.8716766113599643]\\
&\cdot[\hat{r}\cdot(\hat{r} - 2.50290548851635) + 1.668549182690922]\\
&\cdot[\hat{r}\cdot(\hat{r} - 2.0924467509943674) + 1.3150372774478005]\\
&\cdot[\hat{r}\cdot(\hat{r} - 1.564328475106985) + 0.8987511149780485]\\
&\cdot[\hat{r}\cdot(\hat{r} - 1.009780903403673) + 0.5124363774128722]\\
&\cdot[\hat{r}\cdot(\hat{r} - 0.5304054524800665) + 0.2169886022464641]\\
&\cdot[\hat{r}\cdot(\hat{r} - 0.1356566408715063) + 0.035852347523891395]
\end{aligned}$$

and $\hat{r} \equiv r/5$.

$$\begin{aligned}
\phi_{\mathrm{PdPd,u}}(r) &= -79{,}415.24035137112\\
&\cdot(\hat{r} - 1.0699996145674568)\cdot(\hat{r} - 1.06015072612581)\\
&\cdot(\hat{r} - 0.42433991011376526)\cdot(\hat{r} + 0.06169160085238687)\\
&\cdot[\hat{r}\cdot(\hat{r} - 2.0586473420376348) + 1.0683922574015199]\\
&\cdot[\hat{r}\cdot(\hat{r} - 1.6696359816422877) + 0.7337878627470482]\\
&\cdot[\hat{r}\cdot(\hat{r} - 1.1690370066230809) + 0.3909805777737639]\\
&\cdot[\hat{r}\cdot(\hat{r} - 0.2635598721249787) + 0.03355111651491024 5] \quad .
\end{aligned} \tag{A3}$$

Note that embedding energy is expressed in terms of $\hat{\rho} \equiv \rho/50$ and electron density and pair energy are expressed in terms of $\hat{r} \equiv r/5$. This is necessary to improve the precision required by the high order polynomial functions. Eqs. (A2) and (A3) are valid only within the cutoff distance $r_{\mathrm{c,PdPd}} = 5.35$ Å.